DOI:
10.1364/OE.20.011582

Document Version
Publisher's PDF, also known as Version of record

Visualizing breast cancer using the Twente photoacoustic mammoscope: What do we learn from twelve new patient measurements?

M. Heijblom,[1,2,*] D. Piras,[1] W. Xia,[1] J.C.G. van Hespen,[1] J.M. Klaase,[2] F.M. van den Engh,[2] T.G. van Leeuwen,[1,3] W. Steenbergen,[1] and S. Manohar[1]

[1]*Biomedical Photonic Imaging Group, MIRA Institute for Biomedical Technology and Technical Medicine, University of Twente, P.O. Box 217, 7500 AE Enschede, the Netherlands*
[2]*Center for Breast Care, Medisch Spectrum Twente hospital, P.O. Box 50000, 7500 KA, Enschede, the Netherlands*
[3]*Biomedical Engineering and Physics, Academic Medical Center, University of Amsterdam, P.O. Box 2270, 1100 DE Amsterdam, the Netherlands*
[*] *m.heijblom@utwente.nl*

Abstract: We acquired images of breast malignancies using the Twente photoacoustic mammoscope (PAM), to obtain more information about the clinical feasibility and limitations of photoacoustic mammography. Results were compared with conventional imaging and histopathology. Ten technically acceptable measurements on patients with malignancies and two measurements on patients with cysts were performed. In the reconstructed volumes of all ten malignant lesions, a confined region with high contrast with respect to the background could be seen. In all malignant cases, the PA contrast of the abnormality was higher than the contrast on x-ray mammography. The PA contrast appeared to be independent of the mammographically estimated breast density and was absent in the case of cysts. Technological improvements to the instrument and further studies on less suspicious lesions are planned to further investigate the potential of PAM.

OCIS codes: (110.5120) Photoacoustic imaging; (120.3890) Medical optics instrumentation; (170.1610) Clinical applications.

References and links

1. M. T. Tirona, R. Sehgal, and O. Ballester, "Prevention of breast cancer (part I): epidemiology, risk factors, and risk assessment tools," Cancer Invest. **28**(7), 743–750 (2010).
2. W. A. Berg, L. Gutierrez, M. S. NessAiver, W. B. Carter, M. Bhargavan, R. S. Lewis, and O. B. Ioffe, "Diagnostic accuracy of mammography, clinical examination, US, and MR imaging in preoperative assessment of breast cancer," Radiology **233**(3), 830–849 (2004).
3. G. Bergers and L. E. Benjamin, "Tumorigenesis and the angiogenic switch," Nat. Rev. Cancer **3**(6), 401–410 (2003).
4. D. M. McDonald and P. L. Choyke, "Imaging of angiogenesis: from microscope to clinic," Nat. Med. **9**(6), 713–725 (2003).
5. M. Heijblom, J. M. Klaase, F. M. van den Engh, T. G. van Leeuwen, W. Steenbergen, and S. Manohar, "Imaging tumor vascularization for detection and diagnosis of breast cancer," Technol. Cancer Res. Treat. **10**(6), 607–623 (2011).
6. T. Uematsu, S. Yuen, M. Kasami, and Y. Uchida, "Comparison of magnetic resonance imaging, multidetector row computed tomography, ultrasonography, and mammography for tumor extension of breast cancer," Breast Cancer Res. Treat. **112**(3), 461–474 (2008).
7. S. M. van de Ven, S. G. Elias, A. J. Wiethoff, M. van der Voort, T. Nielsen, B. Brendel, C. Bontus, F. Uhlemann, R. Nachabe, R. Harbers, M. van Beek, L. Bakker, M. B. van der Mark, P. Luijten, and W. P. Mali, "Diffuse optical tomography of the breast: preliminary findings of a new prototype and comparison with magnetic resonance imaging," Eur. Radiol. **19**(5), 1108–1113 (2009).
8. A. Gibson and H. Dehghani, "Diffuse optical imaging," Philos. Trans. R. Soc. London, Ser. A **367**, 3055–3072 (2009).

#161771 - $15.00 USD Received 18 Jan 2012; revised 21 Mar 2012; accepted 29 Mar 2012; published 7 May 2012

9. B. W. Pogue, S. D. Jiang, H. Dehghani, C. Kogel, S. Soho, S. Srinivasan, X. M. Song, T. D. Tosteson, S. P. Poplack, and K. D. Paulsen, "Characterization of hemoglobin, water, and NIR scattering in breast tissue: analysis of intersubject variability and menstrual cycle changes," J. Biomed. Opt. **9**(3), 541–552 (2004).
10. Q. Zhu, P. U. Hegde, A. Ricci, Jr., M. Kane, E. B. Cronin, Y. Ardeshirpour, C. Xu, A. Aguirre, S. H. Kurtzman, P. J. Deckers, and S. H. Tannenbaum, "Early-stage invasive breast cancers: potential role of optical tomography with US localization in assisting diagnosis," Radiology **256**(2), 367–378 (2010).
11. Q. Zhu, S. H. Kurtzma, P. Hegde, S. Tannenbaum, M. Kane, M. Huang, N. G. Chen, B. Jagjivan, and K. Zarfos, "Utilizing optical tomography with ultrasound localization to image heterogeneous hemoglobin distribution in large breast cancers," Neoplasia **7**(3), 263–270 (2005).
12. B. A. Brooksby, H. Dehghani, B. W. Pogue, and K. D. Paulsen, "Near-infrared (NIR) tomography breast image reconstruction with a priori structural information from MRI: algorithm development for reconstructing heterogeneities," IEEE J. Sel. Top. Quantum Electron. **9**(2), 199–209 (2003).
13. Q. Q. Fang, J. Selb, S. A. Carp, G. Boverman, E. L. Miller, D. H. Brooks, R. H. Moore, D. B. Kopans, and D. A. Boas, "Combined optical and X-ray tomosynthesis breast imaging," Radiology **258**(1), 89–97 (2011).
14. P. Beard, "Biomedical photoacoustic imaging," Interface Focus **1**(4), 602–631 (2011).
15. S. Mallidi, G. P. Luke, and S. Emelianov, "Photoacoustic imaging in cancer detection, diagnosis, and treatment guidance," Trends Biotechnol. **29**(5), 213–221 (2011).
16. Y. Q. Lao, D. Xing, S. H. Yang, and L. Z. Xiang, "Noninvasive photoacoustic imaging of the developing vasculature during early tumor growth," Phys. Med. Biol. **53**(15), 4203–4212 (2008).
17. J. Yao and L. V. Wang, "Photoacoustic tomography: fundamentals, advances and prospects," Contrast Media Mol. Imaging **6**(5), 332–345 (2011).
18. C. Li and L. V. Wang, "Photoacoustic tomography and sensing in biomedicine," Phys. Med. Biol. **54**(19), R59–R97 (2009).
19. S. A. Ermilov, T. Khamapirad, A. Conjusteau, M. H. Leonard, R. Lacewell, K. Mehta, T. Miller, and A. A. Oraevsky, "Laser optoacoustic imaging system for detection of breast cancer," J. Biomed. Opt. **14**(2), 024007 (2009).
20. T. D. Khokhlova, I. M. Pelivanov, V. V. Kozhushko, A. N. Zharinov, V. S. Solomatin, and A. A. Karabutov, "Optoacoustic imaging of absorbing objects in a turbid medium: ultimate sensitivity and application to breast cancer diagnostics," Appl. Opt. **46**(2), 262–272 (2007).
21. S. Manohar, A. Kharine, J. C. G. van Hespen, W. Steenbergen, and T. G. van Leeuwen, "Photoacoustic mammography laboratory prototype: imaging of breast tissue phantoms," J. Biomed. Opt. **9**(6), 1172–1181 (2004).
22. S. Manohar, A. Kharine, J. C. G. van Hespen, W. Steenbergen, and T. G. van Leeuwen, "The Twente Photoacoustic Mammoscope: system overview and performance," Phys. Med. Biol. **50**(11), 2543–2557 (2005).
23. M. Pramanik, G. Ku, C. H. Li, and L. V. Wang, "Design and evaluation of a novel breast cancer detection system combining both thermoacoustic (TA) and photoacoustic (PA) tomography," Med. Phys. **35**(6), 2218–2223 (2008).
24. J. Jose, S. Manohar, R. G. Kolkman, W. Steenbergen, and T. G. van Leeuwen, "Imaging of tumor vasculature using Twente photoacoustic systems," J. Biophotonics **2**(12), 701–717 (2009).
25. R. A. Kruger, R. B. Lam, D. R. Reinecke, S. P. Del Rio, and R. P. Doyle, "Photoacoustic angiography of the breast," Med. Phys. **37**(11), 6096–6100 (2010).
26. Z. Xie, X. Wang, R. F. Morris, F. R. Padilla, G. L. Lecarpentier, and P. L. Carson, "Photoacoustic imaging for deep targets in the breast using a multichannel 2D array transducer," in *Photonics West - Photons Plus Ultrasound: Imaging and Sensing 2011,* A. Oraevsky, and L. Wang, eds. (SPIE, San-Francisco, 2011), 789907–789901: 789907–789906.
27. S. Manohar, S. E. Vaartjes, J. C. G. van Hespen, J. M. Klaase, F. M. van den Engh, W. Steenbergen, and T. G. van Leeuwen, "Initial results of *in vivo* non-invasive cancer imaging in the human breast using near-infrared photoacoustics," Opt. Express **15**(19), 12277–12285 (2007).
28. D. Piras, W. Xia, W. Steenbergen, T. G. Van Leeuwen, and S. Manohar, "Photoacoustic imaging of the breast using the Twente photoacoustic mammoscope: present status and future perspectives," IEEE J. Sel. Top. Quantum Electron. **16**(4), 730–739 (2010).
29. "The ACR breast imaging reporting and data system (BIRADS)," (American College of Radiology 2003), *www.acr.org* (2011).
30. M. Xu and L. V. Wang, "Universal back-projection algorithm for photoacoustic computed tomography," Phys. Rev. E Stat. Nonlin. Soft Matter Phys. **71**(1), 016706 (2005).
31. T. D. Khokhlova, I. M. Pelivanov, and A. A. Karabutov, "Optoacoustic tomography utilizing focused transducers: the resolution study," Appl. Phys. Lett. **92**(2), 024105 (2008).
32. Y. Xu and L. V. Wang, "Effects of acoustic heterogeneity in breast thermoacoustic tomography," IEEE Trans. Ultrason. Ferroelectr. Freq. Control **50**(9), 1134–1146 (2003).
33. C. Kuhl, "The current status of breast MR imaging. Part I. Choice of technique, image interpretation, diagnostic accuracy, and transfer to clinical practice," Radiology **244**(2), 356–378 (2007).
34. E. P. Friedman, M. A. Hall-Craggs, H. Mumtaz, and A. Schneidau, "Breast MR and the appearance of the normal and abnormal nipple," Clin. Radiol. **52**(11), 854–861 (1997).
35. O. Sarica, E. Zeybek, and E. Ozturk, "Evaluation of nipple-areola complex with ultrasonography and magnetic resonance imaging," J. Comput. Assist. Tomogr. **34**(4), 575–586 (2010).

#161771 - $15.00 USD Received 18 Jan 2012; revised 21 Mar 2012; accepted 29 Mar 2012; published 7 May 2012

36. P. V. van Deventer, "The blood supply to the nipple-areola complex of the human mammary gland," Aesthetic Plast. Surg. **28**(6), 393–398 (2004).
37. S. Ciatto, N. Houssami, A. Apruzzese, E. Bassetti, B. Brancato, F. Carozzi, S. Catarzi, M. P. Lamberini, G. Marcelli, R. Pellizzoni, B. Pesce, G. Risso, F. Russo, and A. Scorsolini, "Categorizing breast mammographic density: intra- and interobserver reproducibility of BI-RADS density categories," Breast **14**(4), 269–275 (2005).
38. P. Taroni, A. Bassi, D. Comelli, A. Farina, R. Cubeddu, and A. Pifferi, "Diffuse optical spectroscopy of breast tissue extended to 1100 nm," J. Biomed. Opt. **14**(5), 054030 (2009).
39. H. E. Daldrup-Link, G. H. Simon, and R. C. Brasch, "Imaging of tumor angiogenesis: current approaches and future prospects," Curr. Pharm. Des. **12**(21), 2661–2672 (2006).
40. P. Taroni, A. Pifferi, G. Quarto, L. Spinelli, A. Torricelli, F. Abbate, A. Villa, N. Balestreri, S. Menna, E. Cassano, and R. Cubeddu, "Noninvasive assessment of breast cancer risk using time-resolved diffuse optical spectroscopy," J. Biomed. Opt. **15**(6), 060501 (2010).
41. J. Holash, S. J. Wiegand, and G. D. Yancopoulos, "New model of tumor angiogenesis: dynamic balance between vessel regression and growth mediated by angiopoietins and VEGF," Oncogene **18**(38), 5356–5362 (1999).
42. P. Taroni, A. Pifferi, E. Salvagnini, L. Spinelli, A. Torricelli, and R. Cubeddu, "Seven-wavelength time-resolved optical mammography extending beyond 1000 nm for breast collagen quantification," Opt. Express **17**(18), 15932–15946 (2009).
43. R. L. van Veen, H. J. Sterenborg, A. Pifferi, A. Torricelli, E. Chikoidze, and R. Cubeddu, "Determination of visible near-IR absorption coefficients of mammalian fat using time- and spatially resolved diffuse reflectance and transmission spectroscopy," J. Biomed. Opt. **10**(5), 054004 (2005).
44. S. Fantini and A. Sassaroli, "Near-infrared optical mammography for breast cancer detection with intrinsic contrast," Ann. Biomed. Eng. **40**(2), 398–407 (2012).
45. A. Cerussi, N. Shah, D. Hsiang, A. Durkin, J. Butler, and B. J. Tromberg, "*In vivo* absorption, scattering, and physiologic properties of 58 malignant breast tumors determined by broadband diffuse optical spectroscopy," J. Biomed. Opt. **11**(4), 044005 (2006).
46. R. Nachabé, D. J. Evers, B. H. W. Hendriks, G. W. Lucassen, M. van der Voort, E. J. Rutgers, M. J. Peeters, J. A. Van der Hage, H. S. Oldenburg, J. Wesseling, and T. J. M. Ruers, "Diagnosis of breast cancer using diffuse optical spectroscopy from 500 to 1600 nm: comparison of classification methods," J. Biomed. Opt. **16**(8), 087010 (2011).
47. J. Wang, P. L. Torng, T. P. Liu, K. L. Chen, and T. T. Shih, "Proton MR spectroscopy in normal breasts between pre- and postmenopausal women: a preliminary study," AJR Am. J. Roentgenol. **190**(2), 505–510 (2008).
48. A. Buehler, A. Rosenthal, T. Jetzfellner, A. Dima, D. Razansky, and V. Ntziachristos, "Model-based optoacoustic inversions with incomplete projection data," Med. Phys. **38**(3), 1694–1704 (2011).
49. Y. Xu, D. Z. Feng, and L. V. Wang, "Exact frequency-domain reconstruction for thermoacoustic tomography--I: Planar geometry," IEEE Trans. Med. Imaging **21**(7), 823–828 (2002).
50. B. T. Cox, S. R. Arridge, K. P. Köstli, and P. C. Beard, "Two-dimensional quantitative photoacoustic image reconstruction of absorption distributions in scattering media by use of a simple iterative method," Appl. Opt. **45**(8), 1866–1875 (2006).
51. Z. Yuan and H. B. Jiang, "Quantitative photoacoustic tomography: recovery of optical absorption coefficient maps of heterogeneous media," Appl. Phys. Lett. **88**(23), 231101 (2006).
52. N. R. Jagannathan, "Breast tissue characterization by *in vivo* Magnetic Resonance Spectroscopy," Spectroscopy **25**, 251–260 (2011).
53. A. E. Cerussi, D. Jakubowski, N. Shah, F. Bevilacqua, R. Lanning, A. J. Berger, D. Hsiang, J. Butler, R. F. Holcombe, and B. J. Tromberg, "Spectroscopy enhances the information content of optical mammography," J. Biomed. Opt. **7**(1), 60–71 (2002).
54. V. Ntziachristos and D. Razansky, "Molecular imaging by means of multispectral optoacoustic tomography (MSOT)," Chem. Rev. **110**(5), 2783–2794 (2010).

Introduction

Breast cancer is one of the most common forms of cancer among females and worldwide each year more than 450,000 women are diagnosed with the disease [1]. Conventional breast imaging techniques, like x-ray mammography and ultrasonography, primarily focus on morphological changes of breast tissue to discriminate benign from malignant tissue. However, sensitivity and specificity numbers for both diagnostic x-ray mammography and ultrasonography do not often exceed 85% [2]. Moreover x-ray mammography uses ionizing radiation and is not reliable in women with dense breasts and ultrasonography is strongly operator dependent [2].

Tumor angiogenesis is a critical process in tumor growth and spread. In angiogenesis, new microscopic blood vessels are formed that feed proliferating tumor cells and thereby support unregulated tumor expansion [3, 4]. Therefore, tumor vascularization is a crucial feature to be included in breast imaging [4]. While various techniques for imaging breast cancer related

#161771 - $15.00 USD Received 18 Jan 2012; revised 21 Mar 2012; accepted 29 Mar 2012; published 7 May 2012

vascularization will be briefly discussed here, reference [5] provides a more complete overview.

One commonly used method that focuses on tumor vascularization is Dynamic Contrast Enhanced MRI (DCE-MRI). The high sensitivity of this technique for detecting breast cancer proves that vascularity can indeed provide additional information about the nature of tissue [6]. However, DCE-MRI suffers from a limited specificity, requires the injection of contrast agents and is relatively expensive [6].

The application of far-red and near-infrared (NIR) light in (non-invasively) visualizing cancer and its associated vasculature is gaining attention due to its ability to provide functional and molecular information without the use of ionizing radiation. In recent studies, it has been shown that optical imaging in the form of diffuse optical tomography (DOT) can indeed visualize breast malignancies [7], primarily because of the high absorption of hemoglobin in the NIR regime. However, DOT suffers from low spatial resolution. At a few centimeters depth, the resolution lies in the range of 3 mm and it worsens with depth [8,9]. Several approaches are being investigated to improve the localization and resolution in DOT including using ultrasound guidance [10, 11], MRI [12] and x-ray mammography [13].

Photoacoustic imaging (PAI) also exploits the high NIR light absorption contrast between benign and malignant tissue, but provides superior resolution arising from ultrasound detection [14–17]. In photoacoustic imaging, nanoseconds pulsed laser light induces ultrasound transients due to the thermoelastic mechanism at optical absorbing sites. The pressure wave propagates to the surface where it is detected using wideband ultrasound detectors [14, 15, 18]. The amplitude of the photoacoustic signal depends on the amount of light absorbed in the object and the distance and material between the object and the detector; the time-of-flight and frequency content depend on the object's position and size, respectively. The detected signal is not the highly scattered light, but the much less scattered ultrasound, and therefore the resolution of PAI is superior to that of pure optical techniques.

In the last years, several groups have studied the feasibility of photoacoustics in breast imaging. Special instruments with different configurations have been developed to get the optimal resolution, imaging depth and contrast in breast tissue phantoms and healthy human subjects [19–26]. Also a few clinical studies have been performed exploring the feasibility of producing high-resolution clinical photoacoustic images arising from tumor vascularization [19, 27]. Our own group developed the Twente Photoacoustic Mammoscope (PAM), to image the breast in transmission mode [22, 28]. In a first pilot study with this system in 2007, it was possible to get technically acceptable measurements on five patients with radiographically proven breast malignancies. Of those, four cases revealed a high photoacoustic contrast with respect to the background associated with tumor related vasculature [27, 28].

We have recently started an extended clinical study using PAM, as a continuation of the study performed in 2007. In the new study, we want to investigate the clinical feasibility of photoacoustic mammography in a larger group of patients with different types of breast lesions. Here we describe the results of the first phase of our study.

Materials and methods

The ethical review board of the Medisch Spectrum Twente (MST) approved the study protocol and informed consent procedure. The study has been registered in the Netherlands Trial Register (NTR) as TC 2945.

Patients

Patients were included from the Center for Breast Care of the Medisch Spectrum Twente hospital in Oldenzaal based on the BI-RADS® (Breast Imaging Reporting and Data System [29]) classification of their lesion. Between December 2010 and April 2011, female patients with a palpable breast lesion that was judged as being highly suspicious for malignancy (BI-RADS 5) on at least one of the conventional imaging modalities, were asked to participate to

#161771 - $15.00 USD Received 18 Jan 2012; revised 21 Mar 2012; accepted 29 Mar 2012; published 7 May 2012

the study. Additionally, a selected number of patients exhibiting signs of cysts (BI-RADS 2) were also included in the study. Inclusion criteria were: 1) age over 18 years and 2) the presence of a palpable BI-RADS 5 lesion or a cyst within an accessible region of the breast. Exclusion criteria were: 1) physical incapability to lie in a prone position for 30 minutes; 2) history of breast surgery or radiation therapy within a period of 5 years prior to this study; 3) history of breast biopsy within a period of 3 months prior to this study; and 4) incapability to give fully informed consent. All patients had to sign an informed consent form prior to the study.

Diagnostic procedure

All patients followed the normal diagnostic pathway at the center for breast care of the MST. A nurse practitioner performed clinical anamnesis and physical examination prior to conventional imaging. Cranio-caudal (cc) and medio-lateral-oblique (mlo) x-ray images of both breasts were made using the Lorad Selenia Full Field Digital Mammography System (Hologic, Bedford, USA). The breasts and axillas were also examined by a radiologist using a Philips IU22 ultrasound machine operating at 15 MHz (Philips Medical Systems, Best, The Netherlands). If the patient met the inclusion criteria and signed an informed consent form, she was measured using PAM in between the ultrasound examination and the ultrasound-guided core needle biopsy. Patients exhibiting signs of cysts did not get a core needle biopsy following the photoacoustic investigation. If additional imaging information was required for a proper diagnosis or treatment planning, patients were scheduled for a pre-operative dynamic contrast enhanced MRI investigation. Both high-resolution, anatomic T2 weighted images and dynamic T1 weighted images before and after gadolinium injection were obtained using a 1.5 Tesla MR system in combination with a 7 channel Sense Breast Coil (Philips Medical Systems, Best, The Netherlands). The x-ray, ultrasound and MRI images were interpreted by a breast imaging radiologist. This radiologist also estimated the lesion size on conventional imaging and the lesion depth on ultrasound imaging.

The Twente photoacoustic mammoscope

The Twente photoacoustic mammoscope (PAM, Fig. 1) is built into a hospital bed on which the patient has to lie in a prone position with her breast pendant through an aperture [22, 28]. The breast is slightly compressed between a glass plate at the cranial side and the ultrasound detector array at the caudal side. The breast is illuminated through the glass plate with light from a Q-switched Nd:YAG laser (Continuum Surelite, California) at 1064 nm with 10 ns pulses at a repetition rate of 10 Hz. The illuminating beam scans a rectangular region across the breast. The photoacoustic signals that are generated are detected with a 1 MHz (130% bandwidth) unfocused 2D ultrasound detector array (Lunar Corporation, General Electric, Wisconsin) with a diameter of 80 mm. The detector's characteristics are described in detail elsewhere [28]. The photoacoustic signals are read into the PC on a dual channel digitizer (National Instruments, NI-5112, 100 MS/s, 8 bits). A Labview program (National Instruments) controls the scan stage movements and the element selection.

Information from the x-ray mammograms and ultrasound images was used to define a region of interest (ROI) on the breast. The ROI was usually chosen in the range of 40x40 mm^2, being a trade-off between scan area and scan time. With this size of the ROI, the total measurement time was always kept shorter than 25 minutes. Uncolored ultrasound gel (Sonogel nr. 3010, Germany) was used for acoustic coupling between the breast and the detector. The breast was slightly compressed to ensure good contact with the detector. At the breast, the laser fluence in the 2.5 cm^2 spot was kept at approximately 25 mJ/cm^2. For each position of the light delivery system within the ROI, the opposite detector element was activated and an average was taken over signals generated by 90 subsequent laser pulses.

#161771 - $15.00 USD Received 18 Jan 2012; revised 21 Mar 2012; accepted 29 Mar 2012; published 7 May 2012

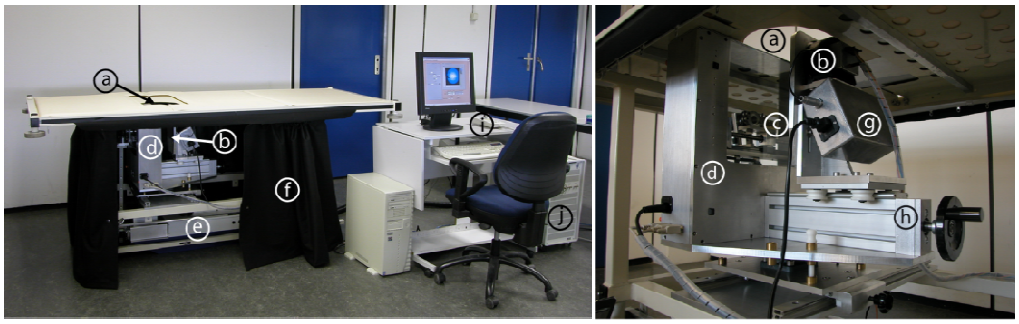

Fig. 1. The Twente photoacoustic mammoscope. **a)** Aperture to insert breast. **b)** Ultrasound detector matrix. **c)** Glass window. **d)** Scanning system compartment. **e)** Q-switched Nd-YAG laser operated at 1064 nm with 10 ns pulses. **f)** Laser safety curtain which is drawn around the instrument during the measurements. **g)** Interface electronics between detector and computer. **h)** Linear stage carrying detector matrix driven by hand wheel to apply mild compression to the breast. **i)** Laser remote control unit. **j)** Laser power supply. Image adapted from reference [27] with permission.

The signal processing and image reconstruction was done with Matlab (R2009b, the Mathworks Company). The offset from all individual signals was removed off-line and the signals were filtered with a low pass Butterworth filter (cut-off frequency 5 MHz) to remove high frequency noise. The prominent breast surface signals were removed from the raw signals prior to reconstruction in order to have a more homogeneous dynamic range in the volume of interest. A modified acoustic backprojection algorithm was used to reconstruct the images. In this algorithm, the signals are back projected over spherical arcs onto their possible points of origin, taking into account the angular sensitivity of the elements [30, 31]. A homogeneous speed of sound (SOS) value of 1540 m/s was chosen for the breast. For the imaging configuration, maximum imaging depth and resolution (3.5 mm in both axial and lateral dimensions [22]) of PAM, the estimated [32] deterioration in resolution is not significant.

After reconstruction, the separate slices were Hilbert transformed and all voxel intensity values were scaled to the maximum intensity value within the total volume, giving a range of intensity values between 0 and 255.

Data analysis

The reconstructed PAM image volumes were analyzed for the presence of confined regions with high intensity. A subvolume was defined as that stack of transverse slices which, on visual inspection, completely included a confined high intensity region. A threshold was chosen to be a percentage (usually 50%) of the maximum intensity value within this subvolume. The photoacoustic abnormality was subsequently defined as that region in which all voxel values exceeded this threshold. The contrast was defined as the ratio of the average intensity value within the abnormality and the average intensity value outside the abnormality. For each abnormality a maximum intensity projection (MIP) image was made. The size was defined as the maximum dimension of the abnormality measured on this MIP image.

The presence, size and shape of the photoacoustic abnormalities was compared with the lesion's appearance and size on conventional imaging as reported by specialized breast radiologists and, if applicable, with the histopathologically (H&E staining) assessed type and size of the lesion (gold standard). The radiologists estimated the depth of the lesion based on the ultrasound images. For each patient, the fibroglandular breast density was then estimated on the x-ray mammogram by a breast radiologist according to the BI-RADS breast density classification scale (Table 1 [29]). Moreover, the contrast of the lesion on x-ray mammography was estimated as the average intensity within an ROI in the malignancy

#161771 - $15.00 USD Received 18 Jan 2012; revised 21 Mar 2012; accepted 29 Mar 2012; published 7 May 2012

divided by the average intensity within an ROI in the background tissue. The breast density was compared with the lesion's contrast seen on both the photoacoustic images and the x-ray mammograms. For both PAM and x-ray mammography, the contrast between the low and high density groups was tested for significant difference using a Student's two-sample t-test.

Table 1. BI-RADS breast density classification scale **[29]**

	Percentage glandular tissue	**Description**
BI-RADS density 1	< 25%	The breast is almost entirely fat
BI-RADS density 2	25-50%	Scattered fibroglandular densities
BI-RADS density 3	51-75%	Heterogeneously dense breasts
BI-RADS density 4	>75%	Extremely dense breasts

Results

In the period December 2010 - April 2011, seventeen Caucasian patients were included in the study. Three patients could not be measured either because of discomfort while lying on the bed or because their lesion was difficult to access completely in the scan region. Of the remaining 14 cases, two were technically unacceptable due to poor acoustic contact between breast and detector in the ROI. Ten of the successful measurements were on highly suspect breasts carrying one or more BI-RADS 5 lesions and two were on breasts with cysts. Table 2 shows an overview of the patients studied.

Table 2. Overview of the patients measured in phase 1 of the study*

The mammographic breast density is expressed as a BI-RADS classification (Table 1). IDC = Infiltrating Ductal Carcinoma and ILC = Infiltrating Lobular Carcinoma. The lesion size is estimated microscopically during histopathological investigation of the tissue specimen post-surgery, the lesion depth is estimated on the ultrasound (US) images as the shortest distance from the skin to the lesion.

Patient	**Age (y)**	**BI-RADS breast density**	**Lesion type**	**Lesion size (histopathology)**	**Lesion depth (US)**
1	78	1	Mixed IDC, ILC	30 mm	< 5 mm
4	67	4	IDC	15 mm	10 mm
5	55	3	ILC	42 mm	10 mm
6	84	3	IDC	13 mm	10 mm
7	57	1	Mixed IDC, ILC	27 mm	13 mm
9	64	2	IDC	31 mm	10 mm
10	49	4	IDC	> 30 mm**	< 5 mm
11	43	4	Cyst	28 mm**	10 mm
14	54	1	IDC	> 40 mm**	< 5 mm
15	48	4	Cyst	42 mm**	5 mm
16	71	2	IDC	33 mm	5 mm
17	68	1	IDC	27 mm	>30 mm

* Only the patient information from the twelve technical acceptable measurements is shown here.
** In patients 10-15, the lesion size was estimated radiologically, since there was no histopathological measurement available.

In the following sections, the results of three representative patient measurements are discussed.

Case 1 – infiltrating ductal carcinoma

In this case, a 67 year old woman (patient 4 in Table 2 and 3) had a palpable lesion in the medial upper quadrant of her right breast. The x-ray image of this lesion is shown in Fig. 2(a). Based on the left-right asymmetry and the presence of a 20 mm lesion (white square) with a suspect calcification in this relatively dense breast tissue, the lesion was judged to be highly suspicious for malignancy (BI-RADS 5). The contrast of the lesion with respect to the fatty tissue was 2.6, while the contrast of the lesion with respect to the fibroglandular tissue was close to 1. The ultrasound image (Fig. 2(b)) showed a 17.5 mm hypoechoic lesion (arrow) 10 mm below the skin. On ultrasound, the lesion was judged as being suspicious for malignancy (BI-RADS 4).

#161771 - $15.00 USD Received 18 Jan 2012; revised 21 Mar 2012; accepted 29 Mar 2012; published 7 May 2012

Transversal slices through the reconstructed photoacoustic volume at the expected lesion depth (Fig. 2(d)) showed the presence of a high-contrast region. Based on the photoacoustic MIP image, the maximum diameter of this abnormality was 10 mm when a 50% threshold was taken to define the abnormality. Figure 2(e) shows a schematic of the imaging planes of the different imaging modalities that are compared throughout this paper. Note that the x-ray, MRI and PAM images are all from the transverse plane; the MRI and PAM images are always rotated to match the orientation of the cranio-caudal x-ray image.

After histopathological confirmation of the presence of an infiltrating ductal carcinoma (IDC), the patient was scheduled for a preoperative MRI. The T2 weighted MRI images showed relatively dense breast structures without cystic changes. T1 post-contrast images confirmed the presence of the malignancy medial in the right breast (white square) with a maximum diameter of 18 mm (Fig. 2(c)). The post-surgical histopathological assessment of the lesion revealed the presence of a 15 mm, grade 2 (on the Bloom-Richardson scale), infiltrating ductal carcinoma.

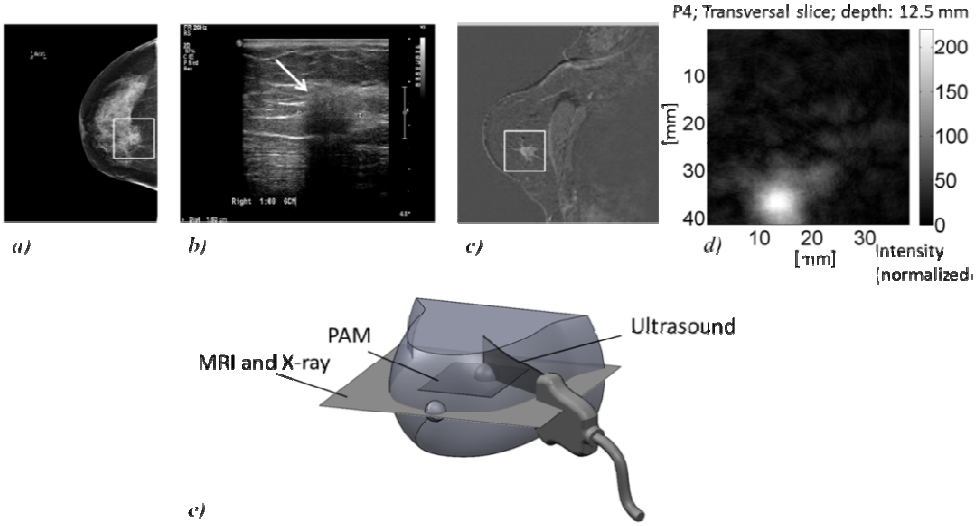

Fig. 2. Case 1: Diagnostic images of a 15mm infiltrating ductal carcinoma in the right breast of a 67 year old woman. **a)** The cranio-caudal (cc) x-ray mammogram shows a 20 mm lesion with a calcification (white box) and is highly suspicious for malignancy. **b)** The ultrasound image shows a 17.5 mm hypoechoic lesion (arrow). **c)** The transverse view of the T1 weighted MRI after gadolinium injection confirms the presence of malignancy because of the enhancement of an 18 mm lesion (white box) in the medial upper quadrant of the right breast. This image is rotated to match the orientation of the cc x-ray view in Fig. 2(a). **d)** A transversal cross-section with a slice-thickness of 0.24 mm through the photoacoustic volume at the expected lesion location shows a confined region with high contrast with respect to the background. With the chosen threshold for abnormality definition, the contrast of the abnormality in the 3D volume is 6.4 and the maximum diameter is 10 mm. This image is rotated to match the orientation of the cc x-ray view in Fig. 2(a). **e)** The imaging planes of the different imaging modalities used in this paper. Indicated are the imaging planes for cranio-caudal x-ray mammography, transverse MRI, transverse PAM and a representative ultrasound view. Imaging planes for MRI, x-ray and PAM are comparable, but the region of interest of PAM is small compared to that of MRI and x-ray, which image the complete breast. The imaging plane of ultrasound is dependent on the position of the ultrasound probe.

Case 2 – ductal carcinoma in situ with infiltrating foci

This 64 year old woman (patient 9 in Table 2 and 3) arrived at the Center for Breast Care following a suspicious screening mammogram. A 50 mm smooth and mobile mass could be palpated in the lateral quadrant of the right breast, which was not directly suggestive for malignancy. The cranio-caudal x-ray image of this patient's right breast (Fig. 3(a)) showed

#161771 - $15.00 USD Received 18 Jan 2012; revised 21 Mar 2012; accepted 29 Mar 2012; published 7 May 2012

atypical and suspicious microcalcifications in the lateral upper quadrant (white square). This area was assigned as BI-RADS 5. The ultrasound images (Fig. 3(b)) showed a large, inhomogeneous abnormality with calcifications in this same region at 9 o'clock (white square). In contrast to the mammogram, the ultrasound image was most suggestive for a benign fibroadenoma. The 30 mm large lesion was judged as BI-RADS 3 (probably benign lesion). Close to this lesion, a comparable, but smaller, lesion could be located (not visible in this image).

The reconstructed photoacoustic volume (Figs. 3(d)-3(f)) showed two abnormalities, separated by less than 10 mm. The contrast and sizes of the lesions can be found in Table 3.

Histopathological assessment of the biopsy revealed signs of ductal carcinoma *in situ* (DCIS) with focalized IDC. A preoperative MRI revealed an extended lobed lesion in the contrast-enhanced T1-weighted images of the right breast in the lateral quadrant (Fig. 3(c), white square). The lesion had a maximum diameter of 34 mm and showed a type 3 enhancement pattern [33] (rapid increase of contrast enhancement with fast wash-out), corresponding to the presence of an infiltrating carcinoma. Caudal to this lesion (not seen in this image) and also in the lateral part of the breast, there was a second lobed lesion with a maximum diameter of 14 mm and also a type 3 enhancement pattern.

Post-surgical histopathological investigation of the breast, revealed the presence of a 31 mm grade 3 IDC growing in irregular fields and associated with extensive DCIS. The two lesions that could be seen on photoacoustic imaging, MRI and US, probably represented two invasive foci of this large abnormal region.

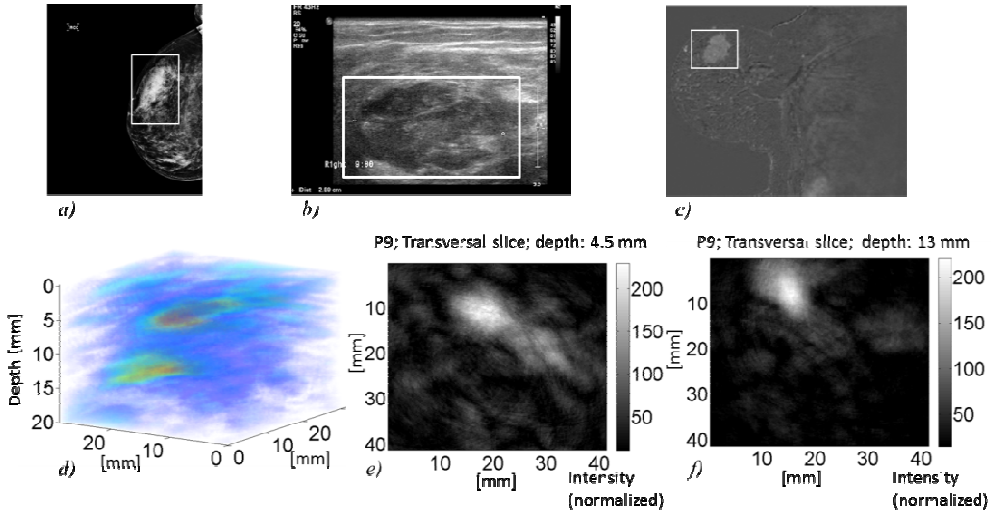

Fig. 3. Case 2: Diagnostic images of a 31 mm infiltrating ductal carcinoma in the right breast of a 64 year old woman. **a)** The cranio-caudal mammogram of the right breast shows a large region with atypical and suspicious microcalcifications (white square). **b)** The ultrasound image shows a large inhomogeneous lobed mass (white square) with microcalcifications, which is somewhat suggestive for a benign fibroadenoma. Close to this large lesion, there is a second comparable, but smaller lesion (not visible in this image). **c)** The T1 weighted contrast enhanced MRI shows two lesions in the lateral quadrant of the right breast. The biggest lesion (white square) is visible in this image and measures 34 mm, the second, smaller lesion (14 mm) is positioned caudal to this lesion and is not visualized here. **d)** Photoacoustic imaging also shows two abnormalities, separated less than 10 mm. **e)** The upper abnormality (5 mm depth) has a contrast of 4.7 and a maximum diameter of 26 mm and can be seen in this transversal cross-section (slice thickness 0.24 mm). **f)** The smaller, lower (13 mm depth) abnormality had a contrast of 5.3 and a maximum diameter of 14 mm.

#161771 - $15.00 USD Received 18 Jan 2012; revised 21 Mar 2012; accepted 29 Mar 2012; published 7 May 2012

Case 3 – mixed infiltrating lobular and ductal carcinoma

This 78 year old woman (patient 1 in Table 2 and 3) had a palpable mass behind the nipple of her left breast. Visual inspection showed reddening and thickening of the skin close to the nipple. On palpation a 20 mm palpable mass could be felt behind this lesion. On x-ray mammography (Fig. 4(a)), the breasts were relatively transparent, but there was a clear left-right asymmetry. Behind the nipple (green square) of the left breast, a region of dense breast tissue (blue-dashed square, lesion 1), associated with some microcalcifications, was identified; this was most likely the palpable lesion. In addition, there was a density close to the nipple (white square, lesion 2), likely the lesion observed on visual inspection. The two lesions were assigned as BI-RADS 4 and BI-RADS 5, respectively. On ultrasound (Fig. 4(b)) only one lesion could be identified: an oval-shaped lesion in the skin just above the nipple (white square). The diameter of this lesion was 18 mm and the lesion was assigned as a BI-RADS 5 lesion. In the remainder of the breast, there were no signs for malignancy.

For photoacoustic imaging, the breast required support by a block and slight tilting to achieve good contact with the detector at the ROI. In contrast to other measurements, the surface signal was not removed before reconstruction, since the most suspicious lesion was positioned close to the breast surface. In Figs. 4(c) and 4(d), two transversal slices through the reconstructed photoacoustic volume are shown. Near the surface a 14 mm abnormality could be observed (Fig. 4(c), white square). In depth, this abnormality was connected to a second abnormality (Fig. 4(d), blue-dashed square). A third region could also be observed at this depth (Fig. 4(d), green-dotted square). We hypothesize that the photoacoustic images show one malignant lesion with a component close to the skin (Fig. 4(c), white square) and a deeper component (Fig. 4(d), blue-dashed square). Please note that by x-ray mammography only two separate lesions and by ultrasonography only one superficial lesion could be observed. The macroscopic and microscopic investigation of the tissue specimen after mastectomy showed indeed one 36 mm, grade 2, mixed infiltrating ductal and lobular carcinoma (mixed IDC and ILC), which was almost attached to the skin of the nipple.

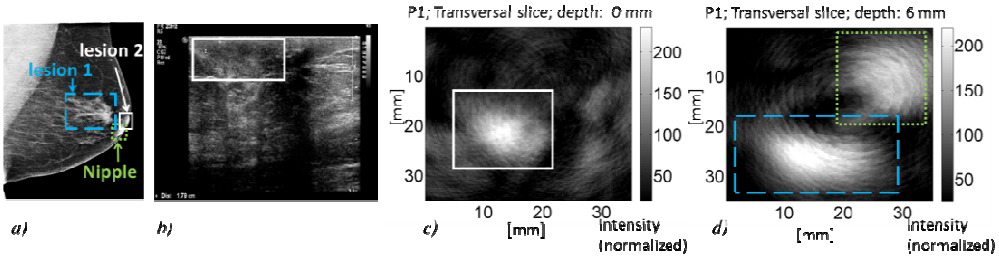

Fig. 4. Case 3: Diagnostic images of a mixed infiltrating ductal and lobular carcinoma in the left breast of a 78 year old woman. **a)** The medio-lateral-oblique x-ray mammogram shows two lesions: a lesion of dense breast tissue (blue-dashed, lesion 1) which is associated with some microcalcifications and is positioned behind the nipple (green dotted square). The second lesion, indicated by a white box, is a density close to the skin of the nipple. **b)** The ultrasound images only show one oval-shaped lesion in the skin just above the nipple (white box). **c)** Transversal cross-sections (slice thickness 0.24 mm) through the photoacoustic image volume show a very superficial 14 mm abnormality (white box), which is attached to the skin and which is in depth connected to **d)** a 15 mm abnormality (blue-dashed square) with a contrast of more than 3 with respect to the background. In this cross-section a third region with high contrast could be observed (green-dotted square), which probably represents the nipple. The circular artifacts that are visible in Figs. 4(c) and 4(d) are inherent to the backprojection algorithm. These artifacts are more pronounced close to the surface as are these slices.

Based on its position in the image, the third region (Fig. 4(d), green-dotted square) was thought to represent the nipple-areola complex. It is known that the nipple-areolar complex also shows contrast enhancement on MRI [34, 35]. This is probably caused by the vascular branches from variable main arteries that supply the nipple-areola complex with blood and nutrients [36]. Therefore, it is plausible that this area is also visible with PAM. Moreover, the

#161771 - $15.00 USD Received 18 Jan 2012; revised 21 Mar 2012; accepted 29 Mar 2012; published 7 May 2012

increased skin pigmentation of the nipple and areola might also absorb the 1064 nm light and thereby contribute to increased signals. To test this hypothesis, the measuring configuration and breast positioning as in patient 1 were repeated with a healthy volunteer. The resulting photoacoustic image (Fig. 5) showed a region of high absorption, highly comparable to the supposed nipple in Fig. 4(d).

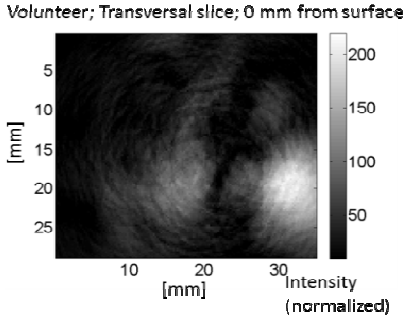

Fig. 5. The photoacoustic image of a healthy volunteer, measured in the same configuration as patient 1. This image shows a transversal cross-section at the position of the nipple. The identified region with high-contrast is quite comparable to the region that was hypothesized to represent the nipple in case 3 (Fig. 4(d), green-dotted square).

Overall results

In the reconstructed volumes of all ten measurements on BI-RADS 5 lesions, a confined region with high contrast with respect to the background could be seen at the depth where the lesion was expected based on the ultrasound images. However, in some patients (patients 5, 6 and 17) this region was at the border of the scan because of slight mispositioning. Incorrect positioning was caused by the limited size of the region of interest. In those patients, the size of the abnormality on the photoacoustic mammogram could not fully be estimated. Table 3 provides an overview of the identified photoacoustic abnormalities with their contrast and size. For comparison, Table 3 also shows the contrast of the lesions on the cranio-caudal x-ray mammograms, and the histopathologically assessed size of the lesions, which is the gold standard for lesion size estimation.

Table 3. Measurement results from photoacoustic mammography

Lesions as defined on the photoacoustic images are compared with x-ray mammography and histopathology, based on contrast and maximum diameter respectively.

Patient	PAM lesion visibility (positive contrast)	PAM lesion contrast	X-ray lesion contrast	PAM max. diameter (50% threshold)	Lesion size (histopathology)
1	Yes	3.2	1.6-4.7**	24 mm	30 mm
4	Yes	6.4	1 –2.6**	10 mm	15 mm
5	Yes	3.3	1.9	***	42 mm
6	Yes	6.2	1.0	***	13 mm
7	Yes	5.3	2.6	14 mm	27 mm
9	Yes, Two lesions	1) 5.3 2) 4.7	3.5	1) 14 mm 2) 26 mm	31 mm
10	Yes	4.5	1.2	13 mm	> 30 mm*
11	No	1.0	1.0	Not visible	28 mm*
14	Yes, scattered abnormality	4.0	3.8	Scattered	> 40 mm*
15	No	1.0	1.0	Not visible	42 mm*
16	Yes.	7.0	3.4	9 mm	33 mm
17	Yes	4.9	1.3	***	27 mm

*In patients 10-15, the lesion size was estimated radiologically, since there was no histopathological measurement available. **These lesions were positioned partly in fatty tissue and partly in fibroglandular tissue. Therefore, the contrast for these lesions on x-ray mammography is given with respect to both types of background. *** In these measurements the defined lesion was only partly positioned within the region of interest and the maximum diameter could not be assessed.

#161771 - $15.00 USD Received 18 Jan 2012; revised 21 Mar 2012; accepted 29 Mar 2012; published 7 May 2012

The two reconstructed volumes of the photoacoustic measurements on cysts (patients 11 and 15) manifested no such confined high-contrast regions which extend over multiple slices in depth. Figure 6(a) shows the photoacoustic imaging results of a 44 year old patient with a cyst (patient 11). On ultrasonography the cyst was estimated to be positioned at more than 10 mm in depth and to measure about 28 mm in diameter. Figure 6(a) shows the non-normalized MIP of the photoacoustic imaging volume in the depth range where the cyst was expected. For comparison, Fig. 6(b) shows a non-normalized MIP from a photoacoustic measurement on a malignancy which was positioned at comparable depth as the cyst. The confined high-contrast area which can clearly be seen in Fig. 6(b) is absent in Fig. 6(a). Despite the fact that both MIPs are taken over the same depth range, the absolute intensity values are lower for the measurement on the cyst than for the measurement on the malignancy.

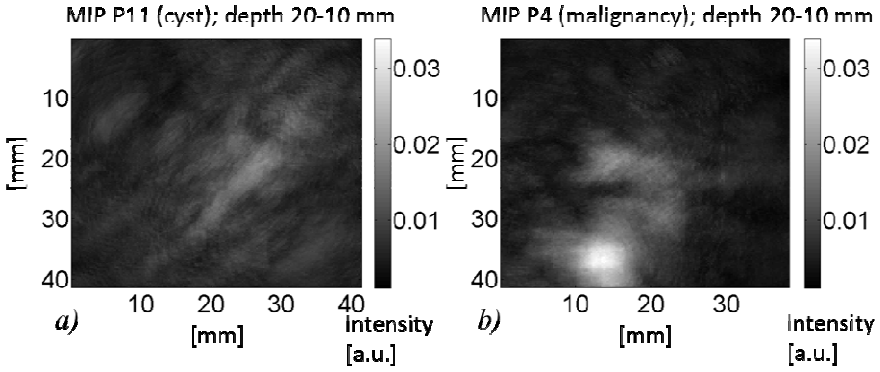

Fig. 6. **a)** Maximum intensity projection (MIP) in cranio-caudal direction of the photoacoustic volume of a patient with a 25 mm cyst. No confined, homogeneous, high-contrast region can be seen. The higher intensities are spread over the complete region of interest. The intensity values are not normalized in this image. **b)** For comparison, a MIP in cranio-caudal direction of the photoacoustic volume of a patient with a malignancy (patient 4, Fig. 2) is visualized. The malignancy is located at a comparable depth as the cyst from Fig. 6(a) and the MIP is taken over the same depth-range. Here a confined high-contrast region can be seen. In the cyst, the non-normalized intensity values are much lower than in the malignancy, despite the fact that the MIPS are from the same depth.

The average contrast for the visible lesions on x-ray mammography and PAM is shown per BI-RADS breast density category in Fig. 7(a). It can be seen that the contrast on PAM is fairly constant with breast density, while the contrast on x-ray mammography decreases for denser breasts. This is more pronounced when a division into two density categories is made (Fig. 7(b)), which is the most reproducible way of grading breast density [37]. The contrast of the lesion on x-ray is statistically different ($p<0.05$) between the high and low density breasts, while there is no statistical difference in the contrast of the lesions on PAM.

#161771 - $15.00 USD Received 18 Jan 2012; revised 21 Mar 2012; accepted 29 Mar 2012; published 7 May 2012

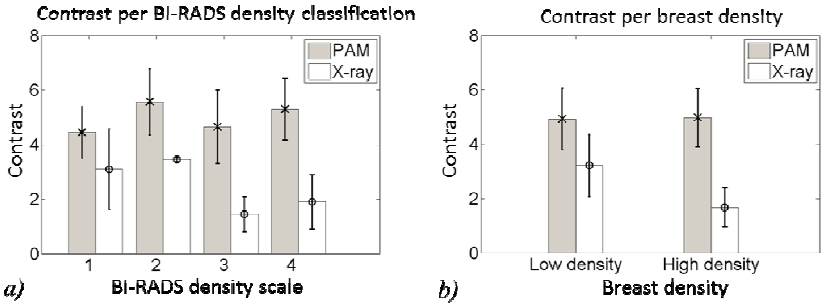

Fig. 7. **a)** Per BI-RADS density classification scale, the average contrast of the lesions on PAM (gray) and x-ray mammography (white) is given. **b)** Here, only a differentiation between 'low' (BI-RADS density 1, 2) and 'high' (BI-RADS density 3, 4) breast density is made. The error bars show the plus and minus one standard deviation. When the lesion was positioned partly in fatty and partly in glandular tissue on the x-ray mammogram (patients 1 and 4), the contrast with respect to the fatty tissue was chosen, which always was the highest contrast.

Discussion

In this study we showed that NIR photoacoustic imaging as embodied in the Twente Photoacoustic Mammoscope (PAM) visualized breast malignancies in women with a high imaging contrast, while cysts did not manifest such confined high-contrast regions. Furthermore, the PAM determined contrast seems to be independent of mammographic breast density. However, PAM determined lesion size seems to be smaller than the histologically determined tumor sizes. Here, we critically discuss the results in the context of instrumental characteristics and limitations.

Contrast and wavelength

Light at 1064 nm is suitable for photoacoustic breast imaging: absorption and scattering are generally lower than at other wavelengths in the optical window, so that light can penetrate deep in breast tissue. Hemoglobin, primarily in its oxygenated variant, absorbs light at 1064 nm [38] and therefore, contrast between healthy and malignant breast tissue is still expected because of the angiogenesis related increase in hemoglobin concentration.

In all ten malignancies, PAM was able to visualize a confined high-contrast region at the true lesion depth and in all cases, the contrast was higher than observed on x-ray mammography. On average, the contrast of the abnormalities on PAM was 5, while the lesions could be seen on x-ray mammography with an average contrast of less than 3. This presence of confined high-contrast regions in photoacoustic images (Figs. 2-4) of malignancies, points to the visualization of the optical properties associated with carcinoma. It is most likely that we are observing, via the absorption of primarily oxyhemoglobin, the host tissue response in the form of angiogenesis [3, 4, 38, 39]. The contrast in our photoacoustic images seems not to be affected by the fibroglandular breast density (see Fig. 7), unlike in x-ray mammography [2]. This can be explained by the expectation that neither the total hemoglobin concentration nor the oxygen saturation is significantly different between the four BI-RADS breast density scales [40].

The appearance of the rather homogeneous high-contrast regions is difficult to attribute solely to oxyhemoglobin, since it is known that the tumor vascularization is inhomogeneous and often more pronounced in the peripheral areas [41]. In addition to oxyhemoglobin at 1064 nm, other important tissue constituents also absorb at this wavelength: water absorption is not low [42] and absorption by lipids and collagen is also not negligible [14, 38, 43]. While the fat content in cancerous tissue is decreased [44, 45], the (free) water concentration is significantly increased in invasive carcinoma compared to the surrounding normal breast

#161771 - $15.00 USD Received 18 Jan 2012; revised 21 Mar 2012; accepted 29 Mar 2012; published 7 May 2012

tissue [45, 46]. A contribution from water absorption to the photoacoustic image intensity cannot be excluded.

Our results indicate that the contribution of water to the photoacoustic contrast is probably small with respect to the contribution of hemoglobin. First, if water was the prominent source of our photoacoustic contrast for breast carcinoma, we would also expect to see high contrast regions in the photoacoustic images of cysts which primarily consist of water. Because of the limited bandwidth of the transducer, the cysts would probably appear edge-enhanced. Though measurements on cysts have to be performed in a larger study population, the two measurements on cysts measured in the first phase of the study manifest no such features (Fig. 6). Second, we would expect to see a decrease in photoacoustic contrast for the higher density breasts as these are associated with a significant increase in water concentration of the background tissue [40, 47]. In our results, the photoacoustic contrast seems to be independent of the breast density instead.

It is therefore likely that the high photoacoustic contrast is the consequence of the combined absorption of predominantly hemoglobin with minor contribution of water in the extracellular tissue matrix. Further research to the specific contributions of all chromophores is required for an optimal discrimination between benign and malignant breast lesions.

Size and shape

The size and shape of the abnormalities estimated from photoacoustic images, deviated from that on conventional imaging and histopathological assessment. There are several factors that can influence the abnormality's appearance.

First, deviations can be the consequence of breast positioning and the amount of compression applied, both are varying between the different imaging modalities. Second, the level of the threshold strongly influences the estimation of the lesion's extension. In Fig. 8 it can, for example, be seen that the lesion's maximum diameter increases from 8 to 20 mm when the threshold decreases from 60% to 20%. Future evaluations in a large number of patients have to be performed to assess the optimal threshold for precise estimation of the true lesion size.

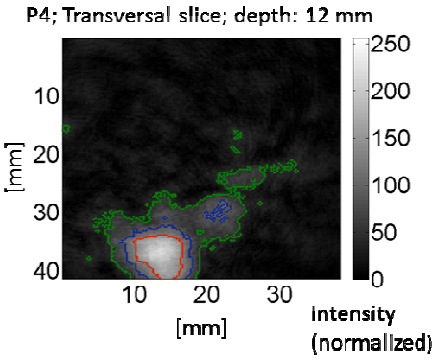

Fig. 8. Transversal cross-section through the photoacoustic mammogram of patient 4 (see Fig. 2). The lesion is defined with the help of three different thresholds, which are all expressed as a percentage of the maximum intensity value (red = 60%, blue = 40% and green = 20%). The value of the threshold strongly influences the maximum diameter of the defined lesion. In this case, the diameter of the lesion is estimated as being 8, 12 and 20 mm for the 60, 40 and 20% threshold respectively.

Further, the planar imaging geometry provides limited views or incomplete tomographic projections for accurate reconstruction of especially size and shape of an abnormality [48, 49]. The viewing angle is further reduced since we consciously make a trade-off between scan area and scan duration in favor of shorter scan duration.

#161771 - $15.00 USD Received 18 Jan 2012; revised 21 Mar 2012; accepted 29 Mar 2012; published 7 May 2012

Finally, what we visualize in our images is not an absolute absorption coefficient, rather the absorbed light energy distribution. Images we obtain are thus affected with depth-dependent falloff in contrast due to optical attenuation. Keeping a constant threshold for boundary estimation in depth can lead to an underestimation of lesion size as observed. A ground truth image contrast distribution and a minimization in the size estimation error can be achieved by using for example a forward model of light transport with iteratively corrected optical properties, that converges to match the reconstructed photoacoustic distribution [50, 51].

Surface signal

Due to the relatively high fluence at the breast surface, a large photoacoustic signal from the surface is present for all signals in the ROI. Therefore, removal of the photoacoustic surface signal from the remainder of the breast signal before the reconstruction is applied, is important. However, sometimes the skin signal cannot clearly be distinguished from the interior signal, especially since the detector has limited bandwidth. Moreover, the optical absorption of the skin, and therefore the resulting photoacoustic signals, can vary between different skin types. An incorrect removal of the surface signal could introduce size and shape errors for tumors close to the skin. This problem makes photoacoustic imaging in transmission mode with a limited bandwidth detector a challenge for superficial tumors (such as in case 3). Imaging in dark-field where the light delivery is not in the direction of ultrasound detection, or imaging in multiple views, would probably overcome this problem.

Outlook

Photoacoustic imaging allows for the visualization of breast malignancies without the use of ionizing radiation as in x-ray mammography or external contrast agents as in contrast enhanced MRI. The images can be obtained with the patient in a comfortable prone position with only minor breast compression. This study also showed some possibilities for improvement of the Twente Photoacoustic Mammoscope in its current configuration.

The photoacoustic contrast at 1064 nm is possibly the consequence of the combined absorption of hemoglobin and water. However, also the fat content, the fat/water ratio and the oxygen saturation are known to be altered at malignant areas [46, 52]. Moreover, premalignant lesions like DCIS, and benign lesions like fibroadenoma seem to be associated with an increased blood volume fraction and water content respectively [46, 53].Those lesions might be differentiated from invasive carcinoma based on the concentrations of other chromophores and the oxygen saturation. The use of multiwavelength strategies will facilitate discrimination between various chromophores [54], which could help in discriminating malignant lesions from premalignant and benign lesions.

In this study we mainly included Caucasian patients with lesions that were highly suspicious for malignancy on conventional imaging. Moreover, our system only allowed us to measure palpable lesions in certain regions of the breast. At last, the small region of interest we can measure within an acceptable time makes positioning difficult and can cause size and shape deviations in the reconstructed volume. Those problems can be overcome by increasing the measurement speed.

PAM can visualize breast lesions with high contrast with respect to the background, but in order to estimate the discriminative power and clinical significance of photoacoustic breast imaging, we should gradually focus on less suspicious lesions, benign lesions and normal breasts with the aforementioned technical improvements.

Conclusions

The current study demonstrates the potential value of photoacoustic imaging of breast tumors. Photoacoustic images showed the lesions with a higher contrast than with x-ray mammography, while cysts did not induce such confined photoacoustic contrast. The

#161771 - $15.00 USD Received 18 Jan 2012; revised 21 Mar 2012; accepted 29 Mar 2012; published 7 May 2012

technique has several advantages over conventional modalities. The method neither uses ionizing radiation, nor contrast agents and seems not to be affected by the fibroglandular breast density. If the measurement speed were increased and complete 3D breast imaging were possible, the added value of photoacoustic imaging in breast diagnosis could be investigated. It is expected that even better contrasts and imaging depths would be obtained with the optimal choice of wavelengths and change of the image configuration.

Conflict of interest

J.v.H., W.S., T.v.L., F.v.d.E. and S.M. have financial interest in PA Imaging Holding BV, which however did not support this work.

Acknowledgments

The financial support of the Agentschap NL Innovation–Oriented Research Programme (IOP) Photonic Devices under the HYMPACT Project (IPD083374); MIRA Institute for Biomedical Technology and Technical Medicine; and the Vernieuwingsimpuls project (*VICI* grant 10831 of the Netherlands Technology Foundation STW*)* of W. S. are gratefully acknowledged. We thank the nurse practitioners, radiologists and nurses from the Center for Breast Care of the Medisch Spectrum Twente for their help with patient inclusion and patient positioning and Ellen ten Tije, MSc, for her help before and during the measurements. Dr. Mariel Brinkhuis from the Laboratorium Pathologie Oost-Nederland is acknowledged for her help and advice regarding the histopathology results.

#161771 - $15.00 USD Received 18 Jan 2012; revised 21 Mar 2012; accepted 29 Mar 2012; published 7 May 2012